# A computational two-scale approach to cancellous bone remodelling

Paul Steinmann, Ina Schmidt, Peter Pivonka, Areti Papastavrou

Steinmann et al. *Advanced Modeling and Simulation in Engineering Sciences(2024)11:13*
https://doi.org/10.1186/s40323-024-00267-1

Advanced Modeling and Simulation in Engineering Sciences

RESEARCH ARTICLE Open Access

# A computational two-scale approach to cancellous bone remodelling

Paul Steinmann[1,2*], Ina Schmidt[1,4], Peter Pivonka[3] and Areti Papastavrou[4]

*Correspondence: paul.steinmann@fau.de
[1]Institute of Applied Mechanics, Universität Erlangen-Nürnberg, Erlangen, Germany
[2]Glasgow Computational Engineering Centre (GCEC), University of Glasgow, Glasgow, UK
[3]Chair of Biomedical Engineering, Queensland University of Technology, Brisbane, Australia
[4]Faculty of Mechanical Engineering, Technische Hochschule Nürnberg, Nuremberg, Germany

**Abstract**

We propose a novel two-scale (meso-macro-scale) approach to computationally capture cancellous bone remodelling allowing for efficient and effective numerical implementation. Therein, the macro-scale is governed by the well-established kinematics and kinetics of one-scale continuum bone remodelling. However, the constitutive behaviour is not postulated phenomenologically at the macro-scale, but rather follows from the meso-scale. There, for the sake of computational efficiency, the trabecular architecture is idealised as a truss network with the cross-sectional area of the trabeculae adapting to mechanical loading. Then, the meso- and the macro-scale are coupled through up- and down-scaling. Computational results on benchmark problems from bio-mechanics demonstrate that the proposed two-scale approach is effective from a modelling perspective and efficient from a computational perspective. In particular, it automatically captures anisotropy resulting from the irregular trabecular architecture at the meso-scale, and, most importantly, enables the direct investigation of different trabecular structures at the meso-scale, thereby serving as a virtual "magnifiying glass". As an outlook, the proposed two-scale approach to cancellous bone remodelling provides an excellent launch pad for further extension, e.g., by considering more complex trabecular architectures and/or through inclusion of micro-scale bone cellular activities.

**Keywords:** Computational bone remodelling, Cancellous bone, Trabecular architecture, Two-scale approach, Anisotropy

## Motivation

It is widely accepted that bone is a living hierarchical material that adapts its internal structure, among others, to mechanical stimuli as evidenced by in-vivo measurements, see, e.g., [5,38,41]. For this remodelling process, osteoclasts and osteoblasts work in a coupled process of bone resorption and subsequent bone formation to repair minor fatigue damages in the tissue and adapt the bone, e.g., to habitual mechanical loading [1,23,33–35]. Understanding and predicting the remodelling process in human bone is critical, for example to determine fracture risk and/or optimising implant and scaffold integration, see, e.g., [50], and treatment methods. This is especially important in case of degenerative diseases such as osteoporosis, where an imbalance between bone formation and resorption leads to bone loss that weakens the bone.

Meslier and Shefelbine recently reviewed the past 50 years of developments of finite element models for bone adaptation [27]. The majority of early bone adaptation models have been formulated as *one-scale* macroscopic models based on the phenomenological theory of adaptive elasticity [8]. In these models mechano-adaptation responses are based on either strain [8] or energy storage density [15–17,47]. In order to overcome the phenomenological nature of the mechano-adaptive evolution law proposed in these early models, efforts have been made to formulate bone adaptation based on the theory of open system thermodynamics [9,21,22]. The latter framework allows to derive the evolution equation for bone mass density (and material orientation) based on thermodynamic system constraints. Several authors applied this theory to simulations of bone remodelling [19,24,30,31,39,45].

However, none of these one-scale approaches explicitly accounts for the highly irregular trabecular architecture of cancellous bone at the meso-scale. In strong contrast, pixel- or voxel-based finite element models in 2D and 3D, respectively, enable for example analysing the purely mechanical behaviour of small cancellous bone specimens [18,29,44]. Especially when generated using $\mu$CT or HR-pQCT measurements, these models prove to be particularly true to the real geometry [4,10,49]. Moreover, the $\mu$CT-generated voxel-based finite element models even allow the detailed simulation of the remodelling of trabecular bone samples, see, e.g., [46]. Nevertheless, approaches explicitly resolving the meso-scale are computationally prohibitive for whole-bone models, and thus only suitable for studying small bone samples. To aim for computational efficiency, some contributions suggest the use of simplified geometries, but either do not consider the remodelling process [3,20], or only account for a single specific trabecular structure [13]. In other studies, the trabecular architectures used are not variable and strongly depend on the macro-scale finite element discretisation or even a regular pattern [26,32].

Attempts to incorporate the multi-scale nature of bone are made, e.g., by [7,11,48] aiming at determining the trabecular structure by solving a material distribution problem based on density-type design variables at the macro- and meso-scale. For given trabecular structure as characterised by $\mu$CT, [14] propose an approach to bone remodelling coupling finite elements at the macro-scale with a neural network that is trained from voxel-based finite element analysis at the meso-scale.

Given this state of affairs, the objective of this contribution is therefore to develop an efficient yet effective, two-scale approach to computationally capturing cancellous bone remodelling. To this end, we combine continuum concepts of bone remodelling at the macro-scale with a model of trabecular bone at the meso-scale. Thereby, to achieve computational efficiency, the sophisticated cancellous architecture is here, however without sacrificing generality, idealised and indeed simplified as a truss network with the cross-sectional area of the trabeculae adapting to the local mechanical stimuli. To concurrently couple the trabecular meso- and the whole-bone macro-scale, we adopt suited up- and down-scaling strategies. To the author's best knowledge, a simlar two-scale approach has not been attempted before.

## Two-scale approach

We propose a two-scale approach (see Fig. 1), where mechano-adaption problems are concurrently considered at the macro- and meso-scale. The kinematics and kinetics at the

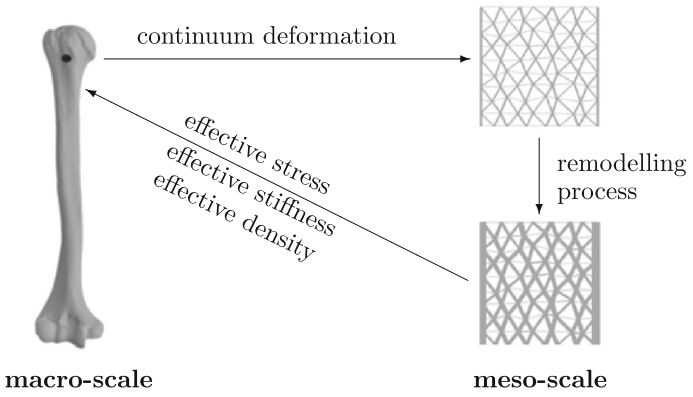


**Fig. 1** Two-scale approach: adaptation of the trabecular geometry at the meso-scale. Mechanobiological feedback is accounted for via the energy storage density in the trabeculae, thereby regulating the phenomenological evolution of the trabecular cross-sections. Effective continuum quantities at the macro-scale, i.e. the stress, stiffness and density, follow via up-scaling from the meso-scale

macro-scale are based on well-established phenomenological continuum bone remodelling, see, e.g., Kuhl and Steinmann [22], where bone is considered a continuum. However, as a novelty, in the current approach the constitutive behaviour is not postulated phenomenologically at the macro-scale, but rather follows directly through up-scaling from the meso-scale. To this end, each (quadrature) point at the macro-scale is assigned a zoom-in volume element (ZVE) representing the trabecular meso-scale structure. The boundary conditions imposed to each ZVE are determined via down-scaling the deformation at the macro-scale. At the meso-scale, for the sake of computational efficiency and simplicity, the cancellous structure is idealised as a trabecular truss network. Through up-scaling, the effective stress, the stiffness and bone density are then transferred back to the macro-scale. The proposed two-scale approach is schematically depicted in Fig. 1 and is discussed in detail in the following sections.

*Notation:* In the sequel we use symbolic tensor notation and avoid entirely any use of matrix notation. Therein, any contraction is indicated by a dot, for example the scalar product of two first-order tensors (vectors) $\boldsymbol{a}$ and $\boldsymbol{b}$ reads $\boldsymbol{a} \cdot \boldsymbol{b}$, the scalar product of two second-order tensors $\boldsymbol{A}$ and $\boldsymbol{B}$ reads $\boldsymbol{A} : \boldsymbol{B}$, and the map of a first-order tensor $\boldsymbol{b}$ into a first-order tensor $\boldsymbol{a}$ by a second-order tensor $\boldsymbol{A}$ reads $\boldsymbol{a} = \boldsymbol{A} \cdot \boldsymbol{b}$.

### Macro-scale continuum model

At the macro-scale, we consider bone as continuous matter [22,30,31,39,40], i.e. in terms of *effective* continuum quantities that do not explicitly resolve any meso-scale features. We here adopt a well-established geometrically nonlinear continuum formulation for the sake of modelling rigour, nevertheless, for the range of deformations expected for hard bone tissue exposed to habitual mechanical loading, the response will automatically approach the geometrically linear limit. We here opt for the well-established geometrically nonlinear remodelling framework from [22] since it does not pose any additional challenges. Thus, without loss of continuum modelling accuracy, we refrain from first unnecessarily linearising it to a geometrically linear formulation. All continuum quantities at the macro-scale are indicated by an overbar.

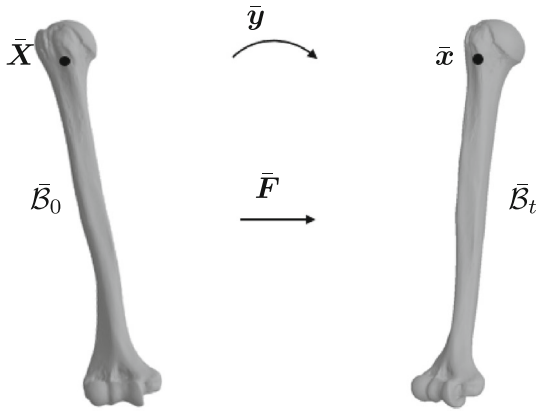


**Fig. 2** Kinematics at macro-scale: material configuration (left) and spatial configuration (right)

*Kinematics:* The kinematics at the macro-scale are characterised by the nonlinear deformation map $\bar{\boldsymbol{y}}$ relating the placement $\bar{\boldsymbol{X}}$ of a continuum point in the material configuration $\bar{\mathcal{B}}_0$ to its position $\bar{\boldsymbol{x}}$ in the spatial configuration $\bar{\mathcal{B}}_t \subset \mathbb{E}^d$ (see Fig. 2)

$$\bar{\boldsymbol{x}} = \bar{\boldsymbol{y}}(\bar{\boldsymbol{X}}, \bar{t}) : \bar{\mathcal{B}}_0 \times \mathbb{R}_+ \to \bar{\mathcal{B}}_t \,. \tag{1}$$

Here $\bar{t}$ denotes the macro-scale time that shall coincide with the meso-scale time, thus $\bar{t} \equiv t$.

The material gradient of the deformation map is denoted the deformation gradient $\bar{\boldsymbol{F}}$

$$\bar{\boldsymbol{F}} = \overline{\mathrm{Grad}}\bar{\boldsymbol{y}}(\bar{\boldsymbol{X}}, \bar{t}) : T\bar{\mathcal{B}}_0 \to T\bar{\mathcal{B}}_t \,, \tag{2}$$

The differential operator $\overline{\mathrm{Grad}}$ expresses the gradient in terms of derivatives with respect to the material coordinates $\bar{\boldsymbol{X}}$. The deformation gradient $\bar{\boldsymbol{F}}$, a two-point tensor, linearly maps from the material tangent space $T\bar{\mathcal{B}}_0$ to the spatial tangent space $T\bar{\mathcal{B}}_t$ at the macro-scale.

*Kinetics:* The kinetics at the macro-scale are collectively dictated by the balances of mass and linear momentum [21]

$$\dot{\bar{\rho}}_0 = \bar{R}_0 \quad \text{and} \quad \overline{\mathrm{Div}}\bar{\boldsymbol{P}} = \boldsymbol{0} \,, \tag{3}$$

with the (effective) nominal mass density $\bar{\rho}_0$ per unit volume in $\bar{\mathcal{B}}_0$, corresponding mass source $\bar{R}_0$, and Piola stress $\bar{\boldsymbol{P}}$ (a two-point tensor mapping from $T^*\bar{\mathcal{B}}_0$ to $T^*\bar{\mathcal{B}}_t$, the material and spatial cotangent spaces), respectively. The differential operator $\overline{\mathrm{Div}}$ expresses the divergence in terms of derivatives with respect to the material coordinates $\bar{\boldsymbol{X}}$ at the macro-scale.

Body forces and inertia are here neglected due to the different levels of gravitational and habitual mechanical loading as well as due to the different time scales of the macro-scale problem and the bone remodelling process.

*Constitutive Expression:* A traditional one-scale phenomenological bone remodelling approach [22,30,31,39,40] requires a constitutive model that expresses the mass source

(for example as in Harrigan and Hamilton [15]) and the Piola stress (for example as a Neo-Hookean response) in terms of the nominal mass density and the deformation gradient, i.e.

$$\bar{R}_0 = \bar{R}_0(\bar{\rho}_0, \bar{\boldsymbol{F}}) \quad \text{and} \quad \bar{\boldsymbol{P}} = \bar{\boldsymbol{P}}(\bar{\rho}_0, \bar{\boldsymbol{F}})\,. \tag{4}$$

In our two-scale approach, however, the density evolution in Eq. 3.1 (and thus the constitutive model in Eq. 4.1) as well as the constitutive model in Eq. 4.2 (together with its consistent linearisation $\bar{\boldsymbol{A}}$ so that $\mathrm{d}\,\bar{\boldsymbol{P}} = \bar{\boldsymbol{A}} : \mathrm{d}\,\bar{\boldsymbol{F}}$) are entirely by-passed by resorting to *up-scaling* from the meso-scale (see below)

$$\bar{\rho}_0 = \langle \rho_0 \rangle \quad \text{and} \quad \bar{\boldsymbol{P}} = \langle \boldsymbol{P} \rangle \quad \text{with} \quad \bar{\boldsymbol{A}} = \langle \boldsymbol{A} \rangle\,. \tag{5}$$

Here the macro-scale quantities $\bar{\rho}_0$, $\bar{\boldsymbol{P}}$ and $\bar{\boldsymbol{A}}$ are equated with corresponding averaged values $\langle \rho_0 \rangle$, $\langle \boldsymbol{P} \rangle$ and $\langle \boldsymbol{A} \rangle$ at the meso-scale. The determination of $\langle \rho_0 \rangle$, $\langle \boldsymbol{P} \rangle$ and $\langle \boldsymbol{A} \rangle$ from the meso-scale truss network model is outlined next.

#### Meso-scale truss network model

Each continuum point at the macro-scale is assigned a *zoom-in volume element* (ZVE) detailing the trabecular structure at the meso-scale. Typical ZVEs are schematically depicted for example in Figs. 1 and 3. We use the terminology ZVE rather than the common terminology "representative volume element (RVE)" to appreciate the lacking scale separation between the solution domain of a ZVE at the meso-scale and a continuum point at the macro-scale. Indeed we accept the lack of scale separation to avoid the need to macroscopically resolve the entire cancellous part of a whole-bone specimen in all detail, which unfortunately is prohibitive effort-wise and moreover also deemed unnecessary. Accepting furthermore severe geometric simplifications[1], we here consider the trabecular structure at the meso-scale simply as an idealised geometrically linear trabecular *truss network*[2]. Despite its simplicity this assumption allows already for complex scenarios wherein truss-like trabeculae with (uniformly) evolving cross-section are of different length and orientation, however, possible bending and/or buckling deformations are neglected (which under physiological mechanical loading appears not too much of a restriction). All, admittedly crude, approximations adopted are here assumed for the sake

[1] Indeed, geometrically, cancellous bone is rather characterised by shell-like structures, which, when captured exactly, today still result, however, in a prohibitive computational burden. Resorting to a two-scale approach allows us generically incorporating the architecture of the trabecular structure at the meso-scale and thus requires formulating corresponding evolution equations for its remodelling. Here, for the sake of simplicity and to highlight the methodology, we opted to consider a truss network to characterise the trabecular architecture at the meso-scale. In this case, a phenomenological evolution equation for the truss cross-sections, i.e. *geometrical quantities*, is a natural option with the cross-sectional evolution driven by the energy storage density in the solid skeleton at the meso-scale, see below. We like to stress though that the methodology is neither restricted to more involved trabecular architectures at the meso-scale such as, e.g., composed by shell-like structures, nor to more mechanobiologically inspired driving forces following, e.g., from up-scaling a bone cell population model operating at the underlying micro-scale. Likewise, within individual trabeculae remodelling need not render a uniform change in their geometry. In this regard the advocated truss-network approach is indeed a compromise between accuracy and computational efficiency and is thus considered only a first step towards more realistically capturing the "true" cancellous bone and its adaption to mechanical stimuli. Clearly, any of these extensions that are certainly on our agenda for the future come at the expense of way higher computational costs.

[2] The restriction to a geometrically linear setting is justified by the small level of external loading (as normalised by the bone stiffness) and in addition entirely avoids rather technical and in the current context unnecessary difficulties when formulating geometrically nonlinear truss networks.

of reducing complexity and increasing computational efficiency (and can/will be relaxed in future developments). In the following the employed finite element setting for the truss-network formulation is outlined in all detail for the sake of self-consistency.

*Kinematics:* At the meso-scale, for the sake of computational efficiency, the trabecular structure is described as a truss network where the trabeculae are considered as truss elements with uniform (but adaptable) cross-sectional area that is sufficiently smaller than their length. For the notation and details of truss network kinematics we refer to the appendix.

*Statics:* For a linear elastic truss network the total energy storage in one element reads

$$W^e = w^e V^e = E^{\mathrm{s}} A^e L^e [\epsilon^e]^2/2. \tag{6}$$

Note, due to the (engineering) strain $\epsilon^e$ (defined in the appendix) being constant in an element there is no volume integral appearing over the energy storage density per volume

$$w^e = E^{\mathrm{s}} [\epsilon^e]^2/2, \tag{7}$$

but $w^e$ is rather simply multiplied with the total volume $V^e = A^e L^e$ of an element. Here, $E^{\mathrm{s}}$, $A^e$ and $L^e$ denote the elastic modulus of the solid material that is assumed constant and given for the trabeculae, the uniform element cross-sectional area and the element length, respectively.

Then, the derivative of the total energy storage $W^e$ with respect to the element vector of displacements $\boldsymbol{u}^e$ (defined in the appendix) renders the element vector of internal forces

$$\boldsymbol{n}^e = \partial W^e / \partial \boldsymbol{u}^e = n^e L^e \boldsymbol{b}^e \tag{8}$$

with $\boldsymbol{b}^e$ the element strain-displacement operator (defined in the appendix) and the uniform normal force in an element

$$n^e = E^{\mathrm{s}} A^e \epsilon^e. \tag{9}$$

The element stiffness tensor follows furthermore from linearisation as

$$\boldsymbol{k}^e = \partial \boldsymbol{n}^e / \partial \boldsymbol{u}^e = k^e [L^e]^2 \boldsymbol{b}^e \otimes \boldsymbol{b}^e \tag{10}$$

with the uniform (longitudinal) tangent stiffness of a truss element

$$k^e = [\partial n^e / \partial \epsilon^e]/L^e = E^{\mathrm{s}} [A^e + \epsilon^e \partial A^e / \partial \epsilon^e]/L^e. \tag{11}$$

Note that the element cross-sectional area evolves due to the energy storage density $A^e = A^e(w^e)$, see below. Consequently, with $w^e = w^e(\epsilon^e)$ the cross-sectional area $A^e$ implicitly depends on the strain $\epsilon^e$.

Finally, in the absence of external forces the assembly of all element contributions results in the global residual and its linearisation

$$\boldsymbol{r} = -\bigcup_e \boldsymbol{n}^e \doteq \boldsymbol{0} \quad \text{and} \quad \boldsymbol{k} \doteq \bigcup_e \boldsymbol{k}^e, \tag{12}$$

so that the Newton update for the global vector of displacements $\boldsymbol{u}$ reads

$$\boldsymbol{u} \to \boldsymbol{u} + \boldsymbol{k}^{-1} \cdot \boldsymbol{r}. \tag{13}$$

*Cross-sectional area evolution:* To consider the remodelling process at the meso-scale, some considerations must be made in advance. Previous findings have shown that bone

remodelling changes mainly the size of individual trabeculae, whereas the overall architecture of the trabecular bone at the meso-scale remains mostly the same. Thus, increased mechanical stimulation causes trabeculae to become thicker without changing the actual number of trabeculae and their connectivity [28]. In contrast, bone resorption may completely remove individual trabeculae, resulting in a modified network with reduced connectivity. Accordingly, our meso-scale approach considers the adaption of the cross-sections of individual truss elements to mechanical stimulus. More precisely, truss elements subjected to high mechanical loading become thicker, while truss elements subjected to insufficient mechanical loading become thinner until they may be completely removed[3].

Based on these considerations, we here propose a simple phenomenological evolution equation for the cross-sectional areas in which the energy storage density in a truss element is compared to a so-called attractor state. Similar to the theory of Frost [12] and Skerry [42] regarding a habitual set-point strain, which initiates either bone formation or resorption, the meso-scale attractor state $w^{\mathrm{a}}$ describes the biological homeostasis to which the system is driving. With this, we model the temporal change in cross-sectional area $\dot{A}^e$ as

$$\dot{A}^e = R^e \quad \text{with} \quad R^e := c\, A^e [w^e - w^{\mathrm{a}}], \tag{14}$$

with the parameter $c$ (dimension volume per energy and time) controlling the velocity of the remodelling process. Note that evolution equation Eq. (14) is the simplest possible approach and can be easily extended, for example by including the activity of osteocytes and and osteoblasts at the cellular scale [33–35].

The temporal discretisation of the cross-sectional area evolution equation over a time step $\Delta t$ is performed with the implicit Euler time stepping scheme. Suppressing explicit indication of the new time point $t_{n+1}$, the time discrete evolution of Eq. (14) reads as

$$\Delta A^e - \Delta t\, R^e(A^e, \epsilon^e) \doteq 0. \tag{15}$$

The linearisation of the updated $A^e$ with respect to $\epsilon^e$ as needed in the expression for the (longitudinal) tangent stiffness $k^e$ of a truss element results eventually as

$$\partial A^e / \partial \epsilon^e = \delta_{\mathrm{A}}\, \partial R^e / \partial \epsilon^e \quad \text{with} \quad \delta_{\mathrm{A}} = [1 - \Delta t\, \partial R^e / \partial A^e]^{-1} \Delta t. \tag{16}$$

Here, concretely, $\partial R^e / \partial A^e = c\,[w^e - w^{\mathrm{a}}]$ and $\partial R^e / \partial \epsilon^e = c\, E^{\mathrm{s}} A^e \epsilon^e = c\, n^e$.

Next, we detail the down- and up-scaling between macro- and meso-scale.

*Down-Scaling:* To relate the macro- to the micro-scale, we impose affine displacement boundary conditions, i.e. prescribed boundary displacements[4] to the ZVE see Fig. 3.

[3] We emphasize that the constitutive equations employed at the meso-scale are inspired by - but not the same as those usually used at the macro-scale. In a one-scale approach the evolution of the bone mass density, a *state quantity* at the macro-scale, is considered. In the two-scale approach the evolution of truss cross-sections, *geometrical quantities* at the meso-scale, is considered whereby the nominal bone mass density at the macro-scale follows as a post-processed quantity from up-scaling. These are two rather different concepts even if the evolution equations at macro- and meso-scale share formal similarities. The orientation of individual trabeculae (before deformation) is admittedly unaffected by the present idealised approach. Potential re-orientations of trabeculae due to remodelling are here, however, deemed a secondary effect, given the geometric simplifications made anyway.

[4] It is noted that other boundary conditions for the ZVE are indeed possible, among them the limiting cases of Voigt and Reuss bounds, traction boundary conditions, as well as the perhaps most accurate, periodic boundary conditions. For a more in-depth discussion we refer to [36] and references therein. Displacement boundary conditions are here merely chosen for the sake of simplicity and demonstration, however without loss of generality. Both traction and periodic boundary conditions require more technicalities when it comes to their implementation, see e.g. our review paper on computational homogenisation [36] among many other accounts on the matter, but do not pose conceptual difficulties per se. It is acknowledged that the selection of either displacement, periodic, or traction boundary conditions results in an effective up-scaled response that is either too stiff, believed to be about right, or too soft.

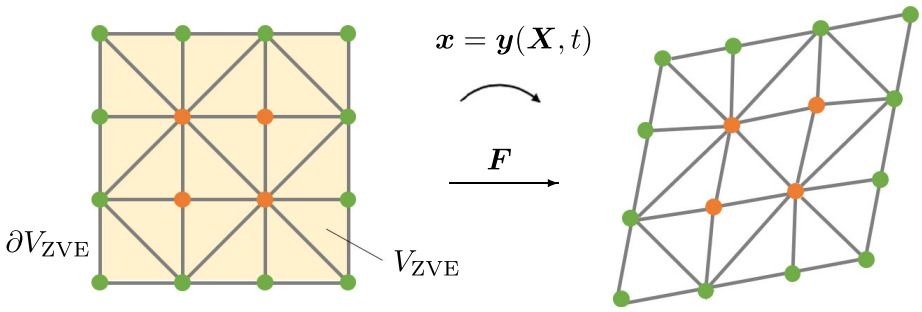


**Fig. 3** Sketch of a ZVE at the meso-scale: material configuration (left) and spatial configuration (right) with retained nodes (filled orange circles) within the ZVE and prescribed nodes (filled green circles) at the boundary of the ZVE

Thereby, the displacements $\boldsymbol{u}_a$ of the truss network node points on the discrete ZVE boundary $\partial V_{\mathrm{ZVE}}$ (constituting the set of boundary node points $\mathcal{N}^{\mathrm{b}}$) are prescribed in terms of the deformation gradient $\bar{\boldsymbol{F}}$ from the macro-scale

$$\boldsymbol{u}_a = \bar{\boldsymbol{F}} \cdot \boldsymbol{X}_a - \boldsymbol{X}_a \quad \forall\, a \in \mathcal{N}^{\mathrm{b}}. \tag{17}$$

With these boundary conditions given, the equilibrium problem for $\boldsymbol{r} \doteq \boldsymbol{0}$ is solved for the displacements $\boldsymbol{u}_a$ of the truss network node points within the ZVE, thus completing the down-scaling.

**Remark:** As an aside, the deformation gradient $\bar{\boldsymbol{F}}$ at the macro-scale relates to the volume average of the deformation gradient $\langle \boldsymbol{F} \rangle$ at the meso-scale as $\bar{\boldsymbol{F}} = \langle \boldsymbol{F} \rangle$, thus

$$\bar{\boldsymbol{F}} = \frac{1}{V_{\mathrm{ZVE}}} \sum_{a \in \mathcal{N}^{\mathrm{b}}} \boldsymbol{y}_a \otimes \boldsymbol{A}_a. \tag{18}$$

Here, $V_{\mathrm{ZVE}}$ represents the volume of the ZVE, see Fig. 3, and $\boldsymbol{A}_a$ denotes the discrete vectorial area element (outwards pointing unit normal multiplied by the discrete area element $A_a$) at boundary node point $a \in \mathcal{N}^{\mathrm{b}}$. □

*Up-Scaling:* To relate the meso- to the macro-scale, first averaged values for the nominal density $\langle \rho_0 \rangle$ and the Piola stress $\langle \boldsymbol{P} \rangle$ are computed for the ZVE

$$\langle \rho_0 \rangle = \frac{V_{\mathrm{T}}}{V_{\mathrm{ZVE}}}\, \rho_0^{\mathrm{s}} \quad \text{and} \quad \langle \boldsymbol{P} \rangle = \frac{1}{V_{\mathrm{ZVE}}} \sum_{a \in \mathcal{N}^{\mathrm{b}}} \boldsymbol{f}_a \otimes \boldsymbol{X}_a. \tag{19}$$

Here $V_{\mathrm{T}} = \sum_{e=1}^{n_{el}} V_e$, $\rho_0^{\mathrm{s}}$ and $\boldsymbol{f}_a$ denote the volume occupied by the trabeculae within the ZVE, the density of the solid material (assumed constant and given for the trabeculae) and the reaction forces (resulting from the assembly of internal forces) at the boundary node points $a \in \mathcal{N}^{\mathrm{b}}$.

Note that for a two-dimensional case we consider the volume $V_{\mathrm{ZVE}}$ and the cross-sectional area $A^e$ as being extruded to the third dimension by assuming a unit thickness.

Then the linearisation of the average Piola stress $\langle \boldsymbol{P} \rangle$ with respect to the deformation gradient at the macro-scale $\bar{\boldsymbol{F}}$, i.e.

$$\mathrm{d}\langle \boldsymbol{P} \rangle = \langle \boldsymbol{A} \rangle : \mathrm{d}\bar{\boldsymbol{F}}, \tag{20}$$

follows in terms of the fourth-order tangent stiffness (or elasticity) tensor

$$\langle \boldsymbol{A} \rangle = \frac{1}{V_{\mathrm{ZVE}}} \sum_{a \in \mathcal{N}^{\mathrm{b}}} \sum_{b \in \mathcal{N}^{\mathrm{b}}} \widehat{\boldsymbol{k}}_{ab} \overline{\otimes} \left[ \boldsymbol{X}_a \otimes \boldsymbol{X}_b \right], \tag{21}$$

which is here denoted (by misuse of the average operator notation) as $\langle \boldsymbol{A} \rangle$. Its detailed derivation is outlined in the appendix.

Finally, the nominal density $\langle \rho_0 \rangle$, the Piola stress $\langle \boldsymbol{P} \rangle$ and its linearisation $\langle \boldsymbol{A} \rangle$ as averaged over the ZVE are equated with their counterparts $\tilde{\rho}_0$, $\tilde{\boldsymbol{P}}$ and $\tilde{\boldsymbol{A}}$ at the macro scale, thus completing the up-scaling.

#### Algorithmic implementation

The algorithmic implementation is based on the previous set of equations. To this end, the finite element method is used for the spatial discretisation at the macro- and the meso-scale. In a nutshell, the step-by-step algorithmic flow follows as

1. The external mechanical load is incremented and applied to the spatially discretised specimen at the macro-scale.
2. The macro-scale deformation gradient $\tilde{\boldsymbol{F}}$ at each macro-scale quadrature point is determined from the macro-scale nodal displacements.
3. The displacements at the boundary of the discrete truss-network ZVE at the meso-scale are prescribed from the macro-scale deformation gradient $\tilde{\boldsymbol{F}}$.
4. The truss network mechano-adaption problem is solved at the meso-scale.
5. The effective stress, nominal bone density, and tangent stiffness tensor are determined from averaging over the ZVE and transferred back to the macro-scale.
6. Using the global (assembled) tangent stiffness at the macro-scale, an iteratively updated estimation of the macro-scale deformation is computed and steps 2–6 are repeated until equilibrium at the macro-scale is obtained.
7. The outer loop starting with step 1 stops at the end of the external load history.

## Benchmark problems

The performance of the proposed two-scale approach is qualitatively demonstrated using two benchmark problems, see, e.g.,Schmidt et al. [40]. These are restricted to two space dimensions for the sake of simplicity and demonstration. The first example considers a uniform macro-scale (unit square) specimen under compression to study the influence of the underlying trabecular truss network structure at the meso-scale. The second example analyses a (two-dimensional) macro-scale proximal femur head under habitual mechanical loading, similar to, e.g., Carter and Beaupré [2], however taking into account the evolving trabecular truss network structure at the meso-scale. Since in both examples the focus of the study is merely on the qualitative behaviour of the two-scale model, all units are omitted. Nevertheless, to qualitatively analyse the evolution of the effective nominal bone density at the macro-scale and the underlying trabecular truss network at the meso-scale, the dimensionless simulation times are also provided.

#### Uniform compression problem

Due to its simplicity, first a uniform (unit square) compression problem is used to study continuum bone remodelling at the elementary level of a single macro-scale point (the quadrature point). Since this homogeneous example has already been considered frequently for the one-scale approach under uniaxial loading in the literature, we consider it a benchmark and chose to compare the results obtained for the two-scale approach for *exactly* the same loading and boundary conditions.

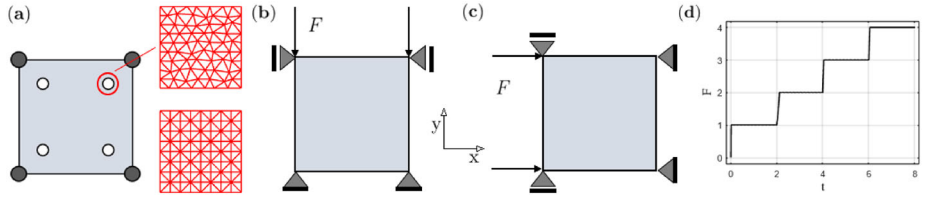


**Fig. 4** Uniform compression problem in 2D: (**a**) a single macro-scale bi-linear finite element with different meso-scale ZVEs representing a structured trabecular truss network (bottom) and an unstructured trabecular truss network (top), (**b**) boundary conditions and mechanical loading in vertical direction, (**c**) boundary conditions and mechanical loading in horizontal direction, (**d**) step-wise increasing mechanical load (forces)

To this end, a single[5] finite element with bi-linear shape functions and $2 \times 2$ Gauss quadrature rule is considered at the macro-scale, see Fig. 4a. Each macro-scale quadrature point is assigned a ZVE at the meso-scale, wherein we analyse two different types of trabecular truss network structures. The structured ZVE consists of 81 equidistantly distributed node points and 208 trabeculae (truss elements) displaying fourfold symmetry horizontally, vertically, and diagonally. The unstructured ZVE consists of 80 node points and 205 trabeculae, wherein node points are randomly shifted. Note that the structured ZVE could be divided into 16 equal unit cells consisting of only 9 node points and 16 trabeculae, however, to better compare it to the unstructured ZVE, we consider the entire ZVE with 81 node points and 208 trabeculae. Moreover, while the number of node points and trabeculae of both ZVEs is similar, the unstructured ZVE results in slightly more node points in vertical than in horizontal direction.

A compressive load in vertical, Fig. 4b, and horizontal direction, Fig. 4c, is applied at the macro-scale node points that increases step-wise over time, Fig. 4d. As a reference, we also considered the entirely phenomenological one-scale continuum bone remodelling approach at the macro-scale as detailed for example in Schmidt et al. [40][6]. The dimensionless set of parameters of the here advocated two-scale approach and of the reference one-scale continuum bone remodelling approach is given in Table 1. Note that we specify an initial (effective) nominal density $\bar{\rho}_0^\star = \bar{\rho}_0(t = 0)$ at time $t = 0$. Consequently, the initial trabecular cross-section area $A^\star = A^e(t = 0)$ is consistently calculated by assuming it initially the same for all trabeculae.

The resulting temporal evolution of the (effective) nominal density $\bar{\rho}_0$ is depicted in Fig. 5a, c. As a trend, initially a lower (effective) nominal density is observed during the first

[5]Since this benchmark problem renders homogeneous response in all macro-scale fields, discretisation by only a single finite element is sufficient. Nevertheless, as a sanity check of our implementation, we confirmed that arbitrary discretisation densities ($1 \times 1$, $2 \times 2$, $3 \times 3$, ... bi-linear elements) result, as expected, in *exactly* the same evolution for the nominal bone mass density and nominal stress components at the macro-scale quadrature points as well as in the same overall displacements.

[6]For the one-scale approach, the relation between the solid and the initial *nominal* material properties is based on the initial volume fraction $\bar{v}_0^\star := \bar{\rho}_0^\star / \rho_0^{\mathrm{s}}$ of the initial nominal density $\bar{\rho}_0^\star$ and the solid bone density $\rho_0^{\mathrm{s}}$, and a homogenisation exponent $\bar{N}$. Then, the current nominal stored energy density follows as $\bar{\psi}_0 = [\bar{v}_0]^{\bar{n}} [\bar{v}_0^\star]^{\bar{N}-\bar{n}} \psi_0^{\mathrm{s}}$ with $\psi_0^{\mathrm{s}}$ the stored energy in the solid bone and $\bar{v}_0 := \bar{\rho}_0 / \rho_0^{\mathrm{s}}$ the current volume fraction. Moreover, the nominal mass source reads as $\bar{R}_0 = \bar{c} \, [\bar{v}_0^{\bar{n}-\bar{m}} [\bar{v}_0^\star]^{\bar{N}-\bar{n}+\bar{m}} \psi_0^{\mathrm{s}} - \bar{\psi}_0^{\mathrm{a}}]$. For the here considered homogenisation exponent $\bar{N} = \bar{n}$ we obtain $\bar{\psi}_0 = [\bar{v}_0]^{\bar{n}} \psi_0^{\mathrm{s}}$ and $\bar{R}_0 = \bar{c} \, [\bar{v}_0^{\bar{n}-\bar{m}} [\bar{v}_0^\star]^{\bar{m}} \psi_0^{\mathrm{s}} - \bar{\psi}_0^{\mathrm{a}}]$, for a detailed derivation and justification of the material parameters selected see Schmidt et al. [40]. The Piola stress entering the macro-scale equilibrium equation then follows as $\bar{\boldsymbol{P}} = [\bar{v}_0]^{\bar{n}} \partial \psi_0^{\mathrm{s}} / \partial \bar{\boldsymbol{F}}$, i.e. as *nonlinearily* (with $\bar{n}$ set to 2 indeed quadratically) scaled by the evolving current volume fraction $\bar{v}_0$. Observe that this is different to the truss normal forces $n^e = E^{\mathrm{s}} \epsilon^e A^e$ that only scale *linearly* with the evolving cross-sectional area $A^e$ in the two-scale approach. Obviously, we can not expect a one-to-one correspondence of the one- and two-scale models, also as the latter incorporates more meso-scale detail.

**Table 1** Uniform compression problem in 2D: dimensionless parameters for the one- and two-scale approach (for the one-scale approach we adopt the model detailed in Schmidt et al. [40])

| | | |
|---|---|---|
| Solid bone Young's modulus | $E^{\mathrm{s}}$ | 10000 |
| Solid bone Poisson's ratio | $\nu^{\mathrm{s}}$ | 0.33 |
| Solid bone density | $\rho_0^{\mathrm{s}}$ | 2 |
| Initial nominal density | $\bar{\rho}_0^{\star}$ | 0.4 |
| One-scale approach exponent | $\bar{m}$ | 3 |
| One-scale approach exponent | $\bar{n}$ | 2 |
| One-scale approach homogenisation exponent | $\bar{N}$ | 2 |
| One-scale approach remodelling velocity factor | $\bar{c}$ | 200 |
| One-scale approach attractor stimulus | $\bar{\psi}_0^{\mathrm{a}}$ | 0.0014 |
| Two-scale approach remodelling velocity factor | $c$ | 133.33 |
| Two-scale approach attractor stimulus | $w^{\mathrm{a}}$ | 0.0056 |

loading phase when comparing the two-scale to the one-scale approach. This behaviour reverts as the load level increases, such that the (effective) nominal density for the two-scale approach is larger at the end of the load history. While the two-scale approach using the structured ZVE responds the same to compression in vertical and horizontal direction, thus indicating isotropic behaviour, compression in vertical direction using the unstructured ZVE here leads to a significantly larger (effective) nominal density than in horizontal direction, thus indicating anisotropic behaviour. Obviously, the anisotropy results from the uneven distribution of node points and truss elements in the vertical and horizontal directions. Indeed, 134 of 205 truss elements experience an increase in cross-sectional area when loaded in vertical direction, whereas only 100 do when loaded in horizontal direction. It is also interesting to observe that the truss elements at the boundary of the unstructured ZVE that are perfectly aligned with either the vertical or horizontal loading direction carry the major part of the load by adapting most, while the internal trusses carry less load and thus also rather reduce their cross-section. As a contrast, for the structured ZVE all trusses aligned with the loading direction, regardless whether at the boundary or inside the ZVE, carry the same load and consequently adapt the same. This may be considered a sanity check.

Considering finally also the displacements at the macro-scale node points in Fig. 5b, d, it is observed that for the presented examples and the chosen material parameters the terminating nodal displacements using the two-scale approach are consistently smaller compared to the one-scale approach; due to the predicted higher (effective) nominal density regardless of the underlying ZVE at the meso-scale.

Note that although the evolution equations for the nominal bone mass density in the one-scale approach and the cross-sectional areas in the two-scale approach share formal similarities, and although the (up-scaled) bone mass density on the macro-scale is similar on average for both approaches, the stresses in the one-scale approach scale nonlinearly (indeed quadratically) with the solid skeleton volume fraction, whereas the truss resultants (forces) scale linearly with the cross-sectional area in the two-scale approach. As a result, we can either tune the two approaches to predict on average similar nominal bone mass density at the macro-scale or to predict on average similar macro-scale displacements (or equivalently effective macro-scale stiffness). Since we are primarily interested in the nominal bone mass density, we here opted for the former.

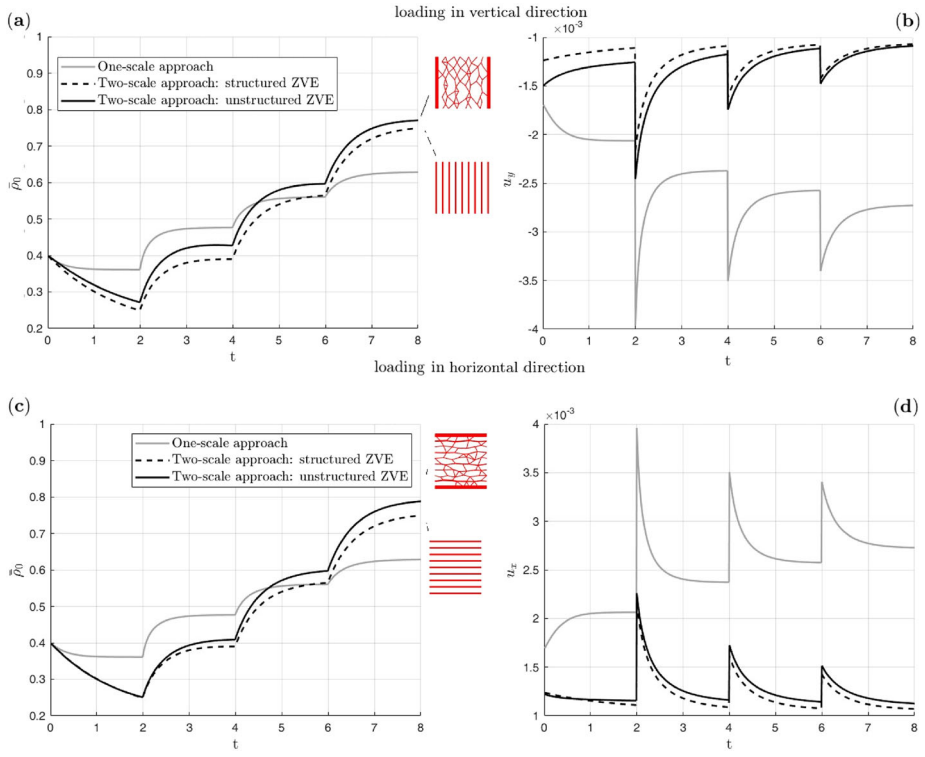


**Fig. 5** Uniform compression problem in 2D: step-wise increased compressive load in (**a**, **b**) vertical and (**c**, **d**) horizontal direction comparing the one- and two-scale approach. (**a**, **c**) temporal evolution of the (effective) nominal density. (**b**, **d**) nodal displacement and terminating trabecular structure at meso-scale for $t = 8$

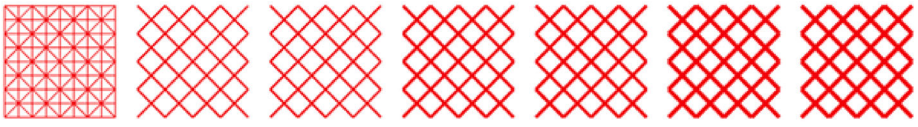

**Fig. 6** Uniform simple shear problem in 2D: the diagonal load-carrying truss elements become thicker while the horizontal and vertical truss elements vanish immediately since they do not carry any load

**Remark:** For the sake of interest and as a sanity check we demonstrate in Fig. 6 the evolution of the cross-sectional areas when employing the structured ZVE in simple shear loading resulting in the diagonal load-carrying truss elements becoming thicker while the horizontal and vertical truss elements vanishing immediately, obviously since they do not carry load in this case.

**Remark:** As a *proof of concept* for the applicability of our two-scale approach to 3D problems we consider the 3D-extension of the above uniform compression problem. For the sake of demonstration we employ a three-dimensional (initially isotropic) bcc-type meso-architecture of the ZVE. Here, the nine nodes of the truss network for the ZVE are positioned at the corners of a unit cube and in its center and are connected by 20 truss elements as showcased in Fig. 7. The macro-scale is discretised by a single tri-linear finite element with the uniform surface load applied in horizontal direction by the same protocol as in Fig. 4d. Fig. 7 displays the evolution of the (effective) nominal density $\bar{\rho}_0$ (panel a) and the evolution of the underlying meso-architecture of the ZVE into an anisotropic structure (panel b). Obviously, the truss elements along the space diagonals and orthogonal to the

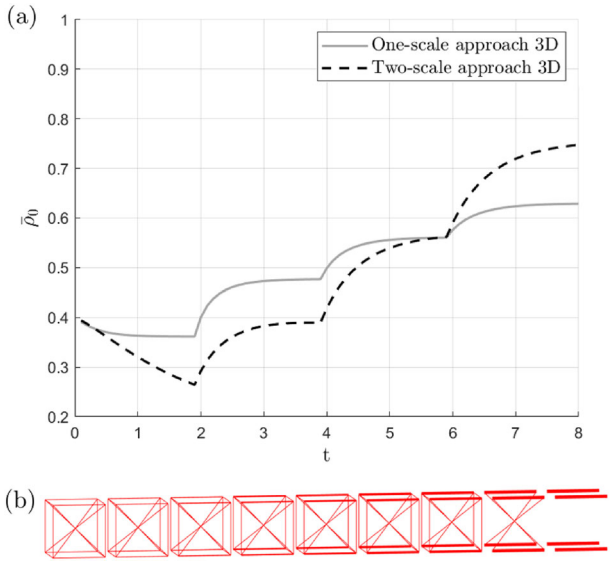


**Fig. 7** Uniform compression problem in 3D: (**a**) temporal evolution of the (effective) nominal density. (**b**) Temporal evolution of the meso-architecture at $t = 0, \cdots, 8$: the horizontal load-carrying truss elements become thicker while the truss elements along the space diagonals and orthogonal to the load direction vanish over time since eventually they do not carry any load

load direction vanish over time while those in load direction considerably increase their cross-sectional area, resulting in the corresponding increase of $\bar{\rho}_0$ (panel a).

#### Proximal femur head

Here, the advocated two-scale approach is applied to a simplified bio-mechanical problem by qualitatively analysing a two-dimensional section of a proximal femur head. The macro-scale finite element mesh consists of 1988 bi-linear continuum elements with $2 \times 2$ Gauss quadrature rule and 2124 node points, see Fig. 8 (left). Consistent linearisation of the averaged Piola stress resulting in Eq. (20) assures a quadratic rate of convergence for the incremental-iterative Newton scheme with only a few iterations in each load increment. Taken together, as a benefit of the severe geometric assumptions regarding the geometry of the underlying trabecular structure, the computational burden of the advocated two-scale approach remains slim.

Habitual daily loading at the femur head can be typified by three characteristic load cases representing the mid-stance, extreme abduction, and extreme adduction phase of the gait cycle. Here, since the accurate determination of the magnitude and spatio-temporal distribution of habitual daily loading as in Christen et al. [6] is not in the scope of this contribution, the loads as detailed in Carter and Beaupré [2] are for simplicity simultaneously applied as single forces at the corresponding node points of the macro-scale discretisation. Obviously, a different mechanical load in terms of magnitude, direction, distribution and location of application critically influences the resulting bone density distribution. The following results are thus merely qualitative at this point and are thus intended to demonstrate the overall applicability, performance and behaviour of the advocated two-scale approach.

Again, the entirely phenomenological one-scale approach detailed in Schmidt et al. [40] serves as reference. To this end, for the one-scale approach, the initial nominal density

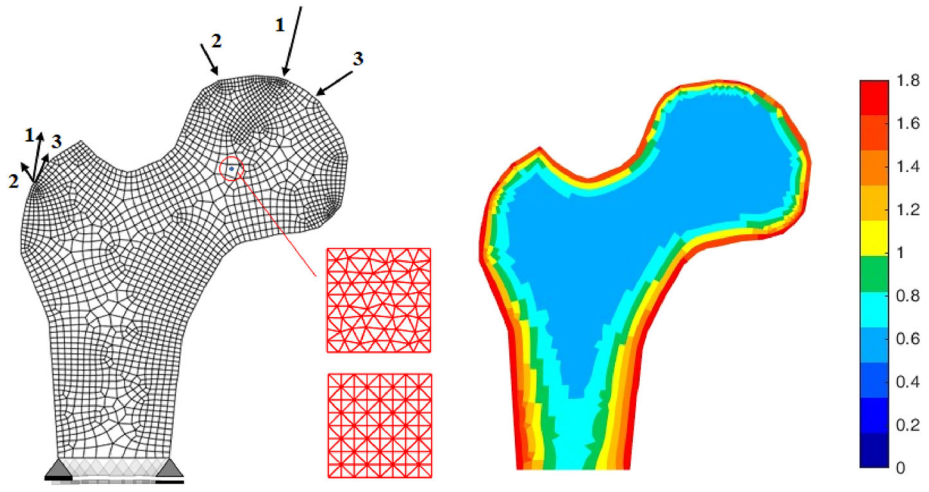


**Fig. 8** Proximal femur head: macro-scale boundary conditions and finite element mesh (left) and the initial (effective) nominal density distribution (right). The cortical bone, i.e. the regions colored from red to yellow, is modelled by the one-scale approach, the trabecular bone, i.e. the regions colored from green to blue, is either modelled by the one-scale or the two-scale approach. For the latter the structured and unstructured ZVEs are considered as displayed (middle)

**Table 2** Proximal femur head: dimensionless parameters for the one- and two-scale approach (for the one-scale approach we adopt the model detailed in Schmidt et al. [40])

| | | |
|---|---|---|
| Solid bone Young's modulus | $E^s$ | 10000 |
| Solid Poisson's ratio | $\nu^s$ | 0.2 |
| Solid bone density | $\rho_0^s$ | 2 |
| Initial nominal density | $\bar{\rho}_0^\star$ | 1.8-0.55 |
| One-scale approach exponent | $\bar{m}$ | 3 |
| One-scale approach exponent | $\bar{n}$ | 2 |
| One-scale approach homogenisation exponent | $\bar{N}$ | 2 |
| One-scale approach remodelling velocity factor | $\bar{c}$ | 1.2 |
| One-scale approach attractor stimulus | $\bar{\psi}_0^a$ | 0.0033 |
| Two-scale approach remodelling velocity factor | $c$ | 0.16 |
| Two-scale approach attractor stimulus | $w^a$ | 0.0233 |

of macro-scale elements at the external boundary is set to $\bar{\rho}_0^\star = 1.8$ representing cortical bone, and to $\bar{\rho}_0^\star = 0.55$ for the internal macro-scale elements representing cancellous bone. A smooth transition zone between cortical bone, including the regions colored from red to yellow in Fig. 8 (right), and cancellous bone, including the regions colored from green to blue in Fig. 8 (right), is represented by a *sigmoidal* function. For the two-scale approach only macro-scale quadrature points with an initial nominal density less than $\bar{\rho}_0^\star = 1$, i.e. only the regions colored from green to blue in Fig. 8 (right), are assigned a ZVE. For these, we again consider either the structured or the unstructured meso-scale ZVE. Thus, macro-scale elements with relatively high initial nominal density representing cortical bone are captured via the one-scale approach, whereas macro-scale elements representing cancellous bone are described either via the one-scale or the novel two-scale approach, thereby considering different ZVEs. The utilised set of dimensionless parameters is given in Table 2.

The evolution of the (effective) nominal density distribution is highlighted for specific simulation time points in Fig. 9. Note that at $t = 0$ the one-scale approach (top row)

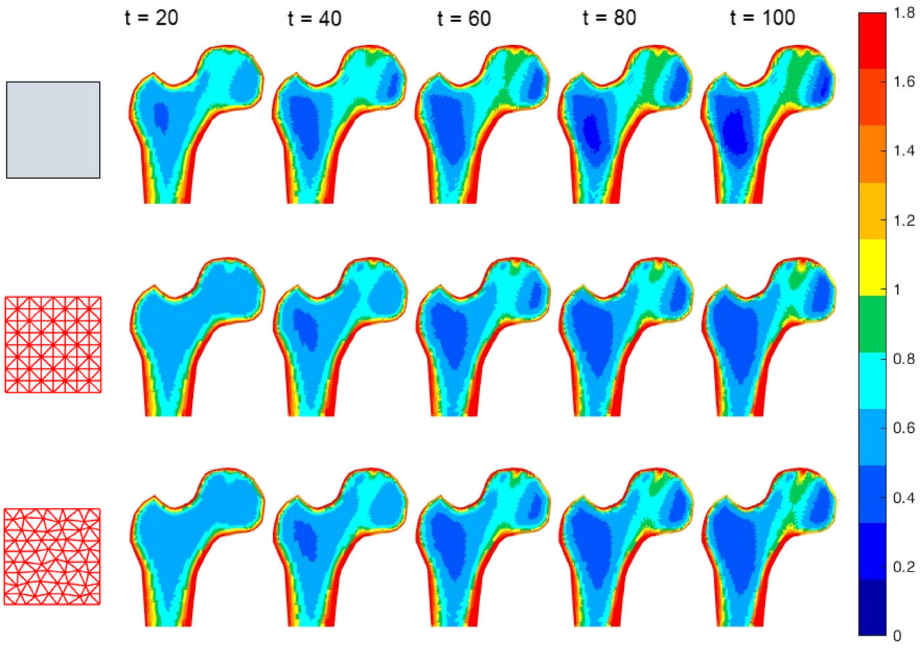


**Fig. 9** Proximal femur head: (effective) nominal density at different time points using the one-scale approach (top row), the two-scale approach with structured ZVE (second row), and the two-scale approach with unstructured ZVE (last row)

and the two-scale approach using either the structured or the unstructured ZVE (second and third row) have the same nominal bone density distribution. However, over time the nominal bone density distribution starts deviating for the different one- and two-scale approaches. Thereby, only small differences are apparent when comparing the results of the two-scale approach with structured and unstructured ZVE in Fig. 9 (second and third row). These minor differences are mainly evident in the highly loaded zone. Overall, however, the (effective) nominal density distribution is pretty similar when comparing the one- and two-scale approaches that consistently predict a slight relative increase in (effective) nominal density in the highly loaded zone on the medial side and reduced bone density in the femoral neck region. Likewise, the cortical bone shell at the boundary of the femur head is predicted as similar.

Nevertheless, using the two-scale approach, we can not only analyse the evolution of the (effective) nominal density, but also, as a virtual "magnifying glass", the evolution of the trabecular structures in the individual ZVEs. To this end, the evolution of the trabecular structures at the meso-scale is exemplified at selected quadrature points of the macro-scale elements A and B, see Fig. 10.

As indicated by the distribution of the (effective) nominal density, macro-scale element B is located in a less loaded region. The (effective) nominal density there decreases from $\bar{\rho}_0^\star = 0.5705$ to $\bar{\rho}_0(t = 100) \approx 0.3959$. Overall thus, the cross-sectional areas of the trabeculae become smaller. Especially when using the structured ZVE, a uniform thinning of the trabeculae over time is evident.

By contrast, when focusing on the macro-scale element A located in a highly loaded region, the dominant load direction is clearly highlighted, as trabeculae lying in this direction become significantly thicker. However, this also entails a thinning of the trabeculae

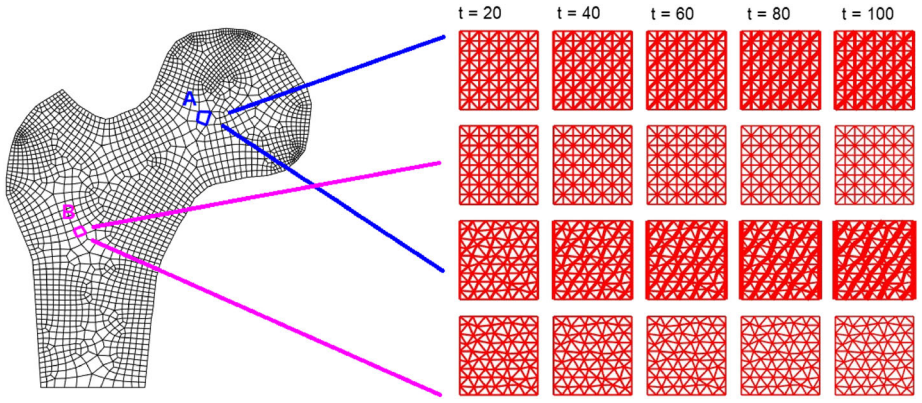


**Fig. 10** Proximal femur head: temporal evolution of the trabecular structure. Structured ZVE at a quadrature point of macro-scale element A highlighted in blue (top row) and of macro-scale element B highlighted in pink (second row). Unstructured ZVE at a quadrature point of macro-scale element A highlighted in blue (third row) and at macro-scale element B highlighted in pink (last row)

perpendicular to this principal loading direction. This effect is especially apparent in the unstructured ZVE. Using the unstructured ZVE thus leads to an increase in (effective) nominal density from $\bar{\rho}_0^\star = 0.5503$ up to $\bar{\rho}_0(t = 100) \approx 0.8030$, whereas the (effective) nominal density only results in $\bar{\rho}_0(t = 100) \approx 0.7867$ when using the structured ZVE.

## Summary and conclusion

A well-established one-scale continuum bone remodelling framework is here extended to a two-scale approach to account in a simple manner for the highly irregular structure of cancellous bone at the meso-scale. The advocated two-scale approach relies on up- and down-scaling without postulating scale-separation when defining the effective response at the macro-scale as resulting from the meso-scale. Here, the rationale is to find a compromise between the prohibitive computational cost when globally resolving the detailed trabecular meso-structure and the attempt to take the trabecular meso-structure into account at least to a certain extent. As a result, we merely consider a zoom-in rather than the common representative volume element. Moreover, within the ZVE the trabecular structure at the meso-scale is idealised and thus severely simplified as a truss network. The energy storage driven evolution of the trabecular cross-sectional area is a consequence of lacking biological homeostasis due to mechanical over- or under-loading. The novel two-scale approach was applied to an elementary uniform and a proximal femur head benchmark problem. Therein, the two-scale approach proved capable to capture the effective macro-scale changes as emerging from bone remodelling at the meso-scale and helps understanding how the structure of the trabecular network affects the effective macro-scale constitutive response. Noteworthy, in this approach anisotropy is a natural outcome as depending on the regular or irregular structure of the trabecular network. Also observe that neither the one-scale approach nor the novel two-scale approach is affected by the widespread numerical checkerboard problem [43], and therefore no smoothing is required in the postprocessing.

Similar to the established one-scale approach to continuum bone remodelling, the novel two-scale approach enables analysing the evolution of the (effective) nominal bone density as response to mechanical over- and under-loading. However, the proposed two-scale

approach also allows analysing the evolution of the trabecular structure at the meso-scale, which is deemed crucial to properly evaluate the quality of bone. As an example, consider the evolution of the trabecular structure in the highly loaded macro-scale region of the femur head benchmark. There, even though the effective nominal density is rather high, the risk of a fracture cannot be precluded, since only the trabeculae in the dominant direction of loading become thicker, whereas the trabeculae perpendicular to this direction display reduced load-carrying capacity. Consequently, despite an overall high effective bone density, the risk of a fracture is increased in case of a sudden change in load direction, which can occur for example in the event of a side-ways fall.

Summarising, the proposed two-scale approach to bone remodelling is effective from a modelling perspective, efficient from a computational perspective, and easily extendable, for example to take the bone cell responses at the cellular scale into account (we will pursue a corresponding three-scale approach in a follow-up contribution, see also Scheiner et al. [37], Martin et al. [25]). The present two-scale approach opens the door to directly investigate and assess various trabecular structures at the meso-scale for the same bone sample at the macro-scale. We thus believe that the proposed two-scale approach provides a promising basis for further development and investigation. However, as of now it still lacks quantitative assessment and can thus not readily translate into clinical practice. To achieve this, we will exploit in a larger collaborative effort medical data-sets for identification and calibration of crucial parameters such as, for example, the here involved meso-scale attractor stimulus.

Taken together, the added value of this contribution is indeed the proposed computationally highly efficient two-scale methodology coupling the discrete trabecular meso-structure of cancellous bone with the evolution of the up-scaled nominal bone mass density at the continuum macro-scale. In particular, even though we here considered elementary truss networks representing the trabecular meso-structure for the sake of computational efficiency and ease of analysis, our advocated two-scale approach is conceptually entirely general and allows considering different meso-structures, including realistic ones obtained from imaging. As an example, the reduction of $\mu$CT images to their skeleton and subsequent discretization as a truss network is on our agenda, again especially for its computational efficiency, and will constitute the topic of a separate contribution. Likewise, extension to open- and/or closed-cell foam-like meso-structures is a valid future possibility, however the increased geometrical complexity comes at elevated computational costs.

**Acknowledgements**
The support of Paul Scheuerlein for the initial 3D implementation is gratefully acknowledged. IS and PS acknowledge support by the Deutsche Forschungsgemeinschaft (DFG, German Research Foundation) under 377472739/GRK 2423/1-2019. AP and IS acknowledge support by the Bavarian Academic Forum (BayWISS) - Doctoral Consortium "Health Research". PP acknowledges support from the Australian Research Council (IC190100020, DP230101404).

**Author contributions**
PS: Conceptualisation, methodology, editing, supervision, funding acquisition. IS: Methodology, implementation, simulations, visualisation, editing. PP: Conceptualisation, methodology, editing, supervision. AP: Conceptualisation, methodology, simulations, visualisation, editing, supervision, funding acquisition.

**Funding**
Open Access funding enabled and organized by Projekt DEAL. IS and PS acknowledge support by the Deutsche Forschungsgemeinschaft (DFG, German Research Foundation) under 377472739/GRK 2423/1-2019. AP and IS acknowledge support by the Bavarian Academic Forum (BayWISS) - Doctoral Consortium "Health Research". PP acknowledges support from the Australian Research Council (IC190100020, DP230101404).

**Availability of data and materials**
All computations were performed using an in-house Matlab code. Input/output data can be made available on request.

## Declarations

**Competing interests**
None of the authors has a financial or personal relationship with other people or organizations that could inappropriately bias his/her work.

## Appendix

Here, for the sake of completeness and in order to fix notation, we detail the underlying kinematics of the truss network model employed as well as the derivation of the fourth-order tangent stiffness tensor.

*Kinematics of truss networks:* A truss network consists of a set of node points $\mathcal{N}$ (globally) numbered by $a = 1, \cdots n_{np}$ connected by elements numbered by $e = 1, \cdots n_{el}$. The coordinates and displacements of the node points are

$$\boldsymbol{X}_a \quad \text{and} \quad \boldsymbol{u}_a \quad \forall\, a = 1, \cdots n_{np}. \tag{22}$$

Node points are assigned to elements via a connectivity list that reads

$$c^e = [a, b] \quad \forall\, e = 1, \cdots n_{el} \quad \text{and} \quad a, b \in \mathcal{N}. \tag{23}$$

Then the element vectors of coordinates and displacements follow as

$$\boldsymbol{X}^e = [\boldsymbol{X}_a \backslash \boldsymbol{X}_b] \quad \text{and} \quad \boldsymbol{u}^e = [\boldsymbol{u}_a \backslash \boldsymbol{u}_b]. \tag{24}$$

Here, for two first-order tensors (vectors) $\boldsymbol{a} \in \mathbb{R}^d$ and $\boldsymbol{b} \in \mathbb{R}^d$ the notation $[\boldsymbol{a} \backslash \boldsymbol{b}] \in \mathbb{R}^{2d}$ refers to a first-order tensor (vector) composed from $\boldsymbol{a}$ and $\boldsymbol{b}$ and mapping from $\mathbb{R}^{2d}$ to $\mathbb{R}$.

Next, with $\boldsymbol{I}$ the second-order unit tensor, we introduce the projection operator

$$\boldsymbol{J} = [-\boldsymbol{I} \mid +\boldsymbol{I}]. \tag{25}$$

Here, for two second-order tensors $\boldsymbol{A} \in \mathbb{R}^d \times \mathbb{R}^d$ and $\boldsymbol{B} \in \mathbb{R}^d \times \mathbb{R}^d$ the notation $[\boldsymbol{A}|\boldsymbol{B}] \in \mathbb{R}^d \times \mathbb{R}^{2d}$ refers to a tensorial object composed from $\boldsymbol{A}$ and $\boldsymbol{B}$ and mapping from $\mathbb{R}^{2d}$ to $\mathbb{R}^d$.

Then the element length and director (a unit vector) follow as

$$L^e = |\boldsymbol{J} \cdot \boldsymbol{X}^e| = |\boldsymbol{X}_b - \boldsymbol{X}_a| \quad \text{and} \quad \boldsymbol{d}^e = \boldsymbol{J} \cdot \boldsymbol{X}^e / L^e. \tag{26}$$

The (engineering) strain in an element, i.e. the elongation of an element divided by its original length, is constant and reads

$$\epsilon^e = \boldsymbol{b}^e \cdot \boldsymbol{u}^e = \boldsymbol{d}^e \cdot [\boldsymbol{u}_b - \boldsymbol{u}_a] / L^e. \tag{27}$$

Here, the strain-displacement operator is defined as

$$\boldsymbol{b}^e = \boldsymbol{d}^e \cdot \boldsymbol{J} / L^e = [-\boldsymbol{d}^e \setminus + \boldsymbol{d}^e] / L^e. \tag{28}$$

Note finally that $[-\boldsymbol{d}^e \setminus + \boldsymbol{d}^e] \cdot \boldsymbol{u}^e = \boldsymbol{d}^e \cdot [\boldsymbol{u}_b - \boldsymbol{u}_a]$.

*Derivation of fourth-order tangent stiffness tensor:* The ZVE tangent stiffness $\boldsymbol{k}$ together with the linearised increments of nodal displacements $\mathrm{d}\boldsymbol{u}$ and nodal forces $\mathrm{d}\boldsymbol{f}$ are partitioned according to the *prescribed* (boundary) nodal displacements at the ZVE boundary and the *retained* (internal) nodal displacements within the ZVE, denoted as $\boldsymbol{u}^{\mathrm{p}}$ and $\boldsymbol{u}^{\mathrm{r}}$, respectively, (see Fig. 3)

$$\begin{bmatrix} \boldsymbol{k}^{\mathrm{rr}} & \boldsymbol{k}^{\mathrm{rp}} \\ \boldsymbol{k}^{\mathrm{pr}} & \boldsymbol{k}^{\mathrm{pp}} \end{bmatrix} \cdot \begin{bmatrix} \mathrm{d}\boldsymbol{u}^{\mathrm{r}} \\ \mathrm{d}\boldsymbol{u}^{\mathrm{p}} \end{bmatrix} = \begin{bmatrix} \boldsymbol{0} \\ \mathrm{d}\boldsymbol{f}^{\mathrm{p}} \end{bmatrix}. \tag{29}$$

Here, $\mathrm{d}\boldsymbol{f}^{\mathrm{p}}$ denotes the linearised increment of the nodal (reaction) forces at the prescribed (boundary) nodes of the ZVE, the corresponding quantities at the retained (internal) nodes are zero to maintain equilibrium. Then, the *reduced* tangent stiffness $\widehat{\boldsymbol{k}}$ relating the linearised increments of the prescribed nodal displacements $\mathrm{d}\boldsymbol{u}^{\mathrm{p}}$ and the corresponding linearised increments of nodal forces $\mathrm{d}\boldsymbol{f}^{\mathrm{p}}$ at the ZVE boundary follows as

$$\widehat{\boldsymbol{k}} = \boldsymbol{k}^{\mathrm{pp}} - \boldsymbol{k}^{\mathrm{pr}} \cdot [\boldsymbol{k}^{\mathrm{rr}}]^{-1} \cdot \boldsymbol{k}^{\mathrm{rp}} \quad \text{so that} \quad \widehat{\boldsymbol{k}} \cdot \mathrm{d}\boldsymbol{u}^{\mathrm{p}} = \mathrm{d}\boldsymbol{f}^{\mathrm{p}} \tag{30}$$

With nodes $a, b \in \mathcal{N}^{\mathrm{b}}$ on the ZVE boundary, the reduced tangent stiffness $\widehat{\boldsymbol{k}}$ as well as $\mathrm{d}\boldsymbol{u}^{\mathrm{p}}$ and $\mathrm{d}\boldsymbol{f}^{\mathrm{p}}$ can be further partitioned into nodal contributions as

$$\widehat{\boldsymbol{k}} = \begin{bmatrix} \widehat{\boldsymbol{k}}_{11} & \cdots & \widehat{\boldsymbol{k}}_{1b} & \cdots \\ \vdots & \ddots & \vdots & \ddots \\ \widehat{\boldsymbol{k}}_{a1} & \cdots & \widehat{\boldsymbol{k}}_{ab} & \cdots \\ \vdots & \ddots & \vdots & \ddots \end{bmatrix}, \quad \mathrm{d}\boldsymbol{u}^{\mathrm{p}} = \begin{bmatrix} \mathrm{d}\boldsymbol{u}_1 \\ \vdots \\ \mathrm{d}\boldsymbol{u}_b \\ \vdots \end{bmatrix} \quad \text{and} \quad \mathrm{d}\boldsymbol{f}^{\mathrm{p}} = \begin{bmatrix} \mathrm{d}\boldsymbol{f}_1 \\ \vdots \\ \mathrm{d}\boldsymbol{f}_a \\ \vdots \end{bmatrix}. \tag{31}$$

Note that the nodal stiffness $\widehat{\boldsymbol{k}}_{ab} \in \mathbb{R}^d \times \mathbb{R}^d$ is a second-order tensor relating the first-order tensors (vectors) $\mathrm{d}\boldsymbol{u}_b \in \mathbb{R}^d$ and $\mathrm{d}\boldsymbol{f}_a \in \mathbb{R}^d$, thus

$$\sum_{b \in \mathcal{N}^{\mathrm{b}}} \widehat{\boldsymbol{k}}_{ab} \cdot \mathrm{d}\boldsymbol{u}_b = \mathrm{d}\boldsymbol{f}_a \quad \forall\, a \in \mathcal{N}^{\mathrm{b}}. \tag{32}$$

With this preliminary at hand, the linearised increment of the averaged Piola stress $\mathrm{d}\langle \boldsymbol{P} \rangle$ follows as

$$\mathrm{d}\langle \boldsymbol{P} \rangle = \frac{1}{V_{\mathrm{ZVE}}} \sum_{a \in \mathcal{N}^{\mathrm{b}}} \mathrm{d}\boldsymbol{f}_a \otimes \boldsymbol{X}_a = \frac{1}{V_{\mathrm{ZVE}}} \sum_{a \in \mathcal{N}^{\mathrm{b}}} \sum_{b \in \mathcal{N}^{\mathrm{b}}} \left[ \widehat{\boldsymbol{k}}_{ab} \cdot \mathrm{d}\boldsymbol{u}_b \right] \otimes \boldsymbol{X}_a. \tag{33}$$

Substituting eventually $\mathrm{d}\boldsymbol{u}_b = \mathrm{d}\bar{\boldsymbol{F}} \cdot \boldsymbol{X}_b$ renders the final expression

$$\mathrm{d}\langle \boldsymbol{P} \rangle = \left[ \frac{1}{V_{\mathrm{ZVE}}} \sum_{a \in \mathcal{N}^{\mathrm{b}}} \sum_{b \in \mathcal{N}^{\mathrm{b}}} \widehat{\boldsymbol{k}}_{ab} \overline{\otimes} \left[ \boldsymbol{X}_a \otimes \boldsymbol{X}_b \right] \right] : \mathrm{d}\bar{\boldsymbol{F}}. \tag{34}$$

Here, the expression in square brackets denotes the required fourth-order tangent stiffness tensor $\langle \boldsymbol{A} \rangle$.

Note the usage of the special dyadic product $\overline{\otimes}$ of two second-order tensors defined as $\left[ \boldsymbol{a} \,\overline{\otimes}\, \boldsymbol{B} \right]_{iJkL} := a_{ik}\, B_{JL}$.

Received: 11 August 2023 Accepted: 16 April 2024
Published online: 23 May 2024

**References**

1. Buenzli PR, Pivonka P, Gardiner BS, Smith DW. Modelling the anabolic response of bone using a cell population model. J Theor Biol. 2012;307:42–52.
2. Carter DR, Beaupré GS. Skeletal function and form: mechanobiology of skeletal development, aging, and regeneration. 1st ed. UK: Cambridge Univ Press; 2001.
3. Cervantes, OR, Schouwenaars R, Ramirez R, Jacobo V, Armando O. Analysis of the architecture and mechanical properties of cancellous bone using 2D voronoi cell based models. In: Proceedings of the World Conference on Engineering. 1. (2010)
4. Chen Y, Dall E, Sales E, Manda K, Wallace R, Pankaj P, Viceconti M, et al. Micro-CT based finite element models of cancellous bone predict accurately displacement once the boundary condition is well replicated: a validation study. J Mech Behav Biomed Mater. 2017;65:644–51.
5. Christen P, Ito K, Ellouz R, Boutroy S, Sornay-Rendu E, Chapurlat RD, Van Rietbergen B. Bone remodelling in humans is load-driven but not lazy. Nat Commun. 2014;5(1):4855.
6. Christen P, Ito K, Santos AAd, Müller R, van Rietbergen B. Validation of a bone loading estimation algorithm for patient-specific bone remodelling simulations. J Biomech. 2013;46(5):941–8.
7. Coelho P, Fernandes P, Rodrigues H, Cardoso J, Guedes J. Numerical modeling of bone tissue adaptation-a hierarchical approach for bone apparent density and trabecular structure. J Biomech. 2009;42(7):830–7.
8. Cowin SC, Hegedus DH. Bone remodeling i: theory of adaptive elasticity. J Elast. 1976;6(3):313–26.

9. DiCarlo A, Naili S, Quiligotti S. Sur le remodelage des tissus osseux anisotropes. Comptes Rendus Mécanique. 2006;334(11):651–61.
10. Du J, Li S, Silberschmidt VV. Remodelling of trabecular bone in human distal tibia: a model based on an in-vivo hr-pqct study. J Mech Behav Biomed Mater. 2021;119: 104506.
11. Fernandes PR, Rodrigues HC, Guedes JM, Coelho PG. Multiscale modelling on bone mechanics-application to tissue engineering and bone quality analysis. IFAC Proc Vol. 2012;45(2):1013–7.
12. Frost HM. Bone mass and the mechanostat: a proposal. Anat Rec. 1987;219(1):1–9.
13. Goda I, Ganghoffer JF. Modeling of anisotropic remodeling of trabecular bone coupled to fracture. Arch Appl Mech. 2018;88:2101–21.
14. Hambli R, Katerchi H, Benhamou CL. Multiscale methodology for bone remodelling simulation using coupled finite element and neural network computation. Biomech Model Mechanobiol. 2011;10(1):133–45.
15. Harrigan TP, Hamilton JJ. Finite element simulation of adaptive bone remodelling: a stability criterion and a time stepping method. Int J Numer Meth Eng. 1993;36(5):837–54.
16. Huiskes R, Weinans H, Grootenboer HJ, Dalstra M, Fudala B, Slooff TJ. Adaptive bone-remodeling theory applied to prosthetic-design analysis. J Biomech. 1987;20(11–12):1135–50.
17. Jacobs CR, Levenston ME, Beaupré GS, Simo JC, Carter DR. Numerical instabilities in bone remodeling simulations: the advantages of a node-based finite element approach. J Biomech. 1995;28(4):449–59.
18. Jang IG, Kim IY. Computational study of Wolff's law with trabecular architecture in the human proximal femur using topology optimization. J Biomech. 2008;41(11):2353–61.
19. Kaczmarczyk L, Pearce C. Efficient numerical analysis of bone remodelling. J Mech Behav Biomed Mater. 2011;4(6):858–67.
20. Kadir MRA, Syahrom A, Ochsner A. Finite element analysis of idealised unit cell cancellous structure based on morphological indices of cancellous bone. Med Biol Eng Comput. 2010;48(5):497–505.
21. Kuhl E, Steinmann P. Mass- and volume-specific views on thermodynamics for open systems. Proc R Soc A Math Phys Eng Sci. 2003;459(2038):2547–68.
22. Kuhl E, Steinmann P. Theory and numerics of geometrically non-linear open system mechanics. Int J Numer Meth Eng. 2003;58(11):1593–615.
23. Lemaire V, Tobin FL, Greller LD, Cho CR, Suva LJ. Modeling the interactions between osteoblast and osteoclast activities in bone remodeling. J Theor Biol. 2004;229(3):293–309.
24. Martin M, Lemaire T, Haiat G, Pivonka P, Sansalone V. Bone orthotropic remodeling as a thermodynamically-driven evolution. J Mech Med Biol. 2020;20(04):1950084.
25. Martin M, Sansalone V, Cooper DML, Forwood MR, Pivonka P. Mechanobiological osteocyte feedback drives mechanostat regulation of bone in a multiscale computational model. Biomech Model Mechanobiol. 2019;18(5):1475–96.
26. Marzban A, Nayeb-Hashemi H, Vaziri A. Numerical simulation of load-induced bone structural remodelling using stress-limit criterion. Comput Methods Biomech Biomed Engin. 2015;18(3):259–68.
27. Meslier QA, Shefelbine SJ. Using finite element modeling in bone mechanoadaptation. Curr Osteoporos Rep. 2023;21(2):105–16.
28. Mittra E, Rubin C, Qin YX. Interrelationship of trabecular mechanical and microstructural properties in sheep trabecular bone. J Biomech. 2005;38(6):1229–37.
29. Oliviero S, Roberts M, Owen R, Reilly G, Bellantuono I, Dall'Ara E. Non-invasive prediction of the mouse tibia mechanical properties from microCT images: comparison between different finite element models. Biomech Model Mechanobiol. 2021;20:941–55.
30. Papastavrou A, Schmidt I, Deng K, Steinmann P. On age-dependent bone remodeling. J Biomech. 2020;103: 109701.
31. Papastavrou A, Schmidt I, Steinmann P. On biological availability dependent bone remodeling. Comput Methods Biomech Biomed Eng. 2020;23(8):432–44.
32. Phillips AT, Villette CC, Modenese L. Femoral bone mesoscale structural architecture prediction using musculoskeletal and finite element modelling. Int Biomech. 2015;2(1):43–61.
33. Pivonka P, Buenzli PR, Scheiner S, Hellmich C, Dunstan CR. The influence of bone surface availability in bone remodelling—a mathematical model including coupled geometrical and biomechanical regulations of bone cells. Eng Struct. 2013;47:134–47.
34. Pivonka P, Zimak J, Smith DW, Gardiner BS, Dunstan CR, Sims NA, John Martin T, Mundy GR. Model structure and control of bone remodeling: a theoretical study. Bone. 2008;43(2):249–63.
35. Pivonka P, Zimak J, Smith DW, Gardiner BS, Dunstan CR, Sims NA, Martin TJ, Mundy GR. Theoretical investigation of the role of the rank-rankl-opg system in bone remodeling. J Theor Biol. 2010;262(2):306–16.
36. Saeb S, Steinmann P, Javili A. Aspects of computational homogenization at finite deformations: a unifying review from Reuss' to Voigt's bound. Appl Mech Rev. 2016; 68(5).
37. Scheiner S, Pivonka P, Hellmich C. Coupling systems biology with multiscale mechanics, for computer simulations of bone remodeling. Comput Methods Appl Mech Eng. 2013;254:181–96.
38. Scheuren AC, Vallaster P, Kuhn GA, Paul GR, Malhotra A, Kameo Y, Müller R. Mechano-regulation of trabecular bone adaptation is controlled by the local in vivo environment and logarithmically dependent on loading frequency. Front Bioeng Biotechnol. 2020;8: 566346.
39. Schmidt I, Albert J, Ritthaler M, Papastavrou A, Steinmann P. Bone fracture healing within a continuum bone remodelling framework. Comput Methods Biomech Biomed Eng. 2022;25(9):1040–50.
40. Schmidt I, Papastavrou A, Steinmann P. Concurrent consideration of cortical and cancellous bone within continuum bone remodelling. Comput Methods Biomech Biomed Eng. 2021;24(11):1274–85.
41. Schulte FA, Ruffoni D, Lambers FM, Christen D, Webster DJ, Kuhn G, Müller R. Local mechanical stimuli regulate bone formation and resorption in mice at the tissue level. PLoS ONE. 2013;8(4): e62172.
42. Skerry TM. One mechanostat or many? Modifications of the site-specific response of bone to mechanical loading by nature and nurture. J Musculoskelet Neuronal Interact. 2006;6(2):122–7.
43. Soffiatti B, Pereira J, Gubaua J, Dicati G. Checkerboard control in 3d analsysis of bone remodelling. 01. 2017.

44. Tsubota K, Suzuki Y, Yamada T, Hojo M, Makinouchi A, Adachi T. Computer simulation of trabecular remodeling in human proximal femur using large-scale voxel FE models: approach to understanding Wolff's law. J Biomech. 2009;42(8):1088–94.
45. Waffenschmidt T, Menzel A, Kuhl E. Anisotropic density growth of bone–a computational micro-sphere approach. Int J Solids Struct. 2012;49(14):1928–46.
46. Wang H, Ji B, Liu XS, Van Oers RF, Guo XE, Huang Y, Hwang KC. Osteocyte-viability-based simulations of trabecular bone loss and recovery in disuse and reloading. Biomech Model Mechanobiol. 2014;13:153–66.
47. Weinans H, Huiskes R, Grootenboer HJ. The behavior of adaptive bone-remodeling simulation models. J Biomech. 1992;25(12):1425–41.
48. Wierszycki M, Szajek K, Łodygowski T, Nowak M. A two-scale approach for trabecular bone microstructure modeling based on computational homogenization procedure. Comput Mech. 2014;54:287–98.
49. Woo DG, Won YY, Kim HS, Lim D. A biomechanical study of osteoporotic vertebral trabecular bone: The use of micro-ct and high-resolution finite element analysis. J Mech Sci Technol. 2007;21(4):593–601.
50. Zhao F, Vaughan TJ, McNamara LM. Quantification of fluid shear stress in bone tissue engineering scaffolds with spherical and cubical pore architectures. Biomech Model Mechanobiol. 2016;15:561–77.

## Publisher's Note